Robust Interfacial Modifier for Efficient Perovskite Solar Cells: Reconstruction of Energy Alignment at Buried Interface by Self-Diffusion of Dopants

Lipeng Wang, Jianxing Xia,* Zheng Yan, Peiquan Song, Chao Zhen, Xin Jiang, Guang Shao, Zeliang Qiu, Zhanhua Wei,* Jianhang Qiu,* and Mohammad Khaja Nazeeruddin*

The under-coordinated defects within perovskite and its relevant interfaces always attract and trap the free carriers via the electrostatic force, significantly limiting the charge extraction efficiency and the intrinsic stability of perovskite solar cells (PSCs). Herein, self-diffusion interfacial doping by using ionic potassium L-aspartate (PL-A) is first reported to restrain the carrier trap induced recombination via the reconstruction of energy level structure at SnO_2/perovskite interface in conventional *n-i-p* structured PSCs. Experiments and theories are consistent with the PL-A anions that can remain at the SnO_2 surface due to strong chemical adsorption. During the spin-coating of the perovskite film, the cations gradually diffuse into perovskite and endow an *n*-doping effect, which provides higher force and a better energy level alignment for the carrier transport. As a result, they obtained 23.74% power conversion efficiency for the PL-A modified small-area devices, with dramatically improved open-circuit voltage of 1.19 V. The corresponding large-area devices (1.05 cm²) achieved an efficiency of 22.23%. Furthermore, the modified devices exhibited negligible hysteresis and enhanced ambient air stability exceeding 1500 h.

1. Introduction

Organic lead halide perovskites (PVK) have proven to be competitive light-harvesting materials for photovoltaic devices owing to their superior photoelectric properties and simple preparation process.[1–6] Within a short period of development, the certified power conversion efficiency (PCE) of perovskite solar cells (PSCs) has soared to 25.7%, making them highly commercially viable.[7] Despite the tremendous progress, they are still dominated by under-coordinated ionic defects in their grain boundaries and contact interfaces, which serve as the non-radiative recombination centre, crucially governing the device performance, stability and hysteresis of PSCs.[8–10] The most efficient SnO_2 based *n-i-p* structured PSCs, surface or bulk vacancies are formed at the surface of metallic oxide SnO_2 and perovskite crystals after PSC fabrication.[11,12] These bulk or interface defects will introduce the defect levels within the bandgap of materials, trapping the free carriers and converting electronic to thermal energy in the contact interfaces and perovskite layers, which significantly reduce the carrier's collection efficiency.[13] Moreover, instability issues rationalized by the severe charge accumulation localized at these defects hinder the formation of stable electric field distribution within devices, presumably resulting in faster degradation of performance and devices hysteresis during the forward-reverse scan.[14,15]

L. P. Wang, C. Zhen, X. Jiang, J. H. Qiu
Shenyang National Laboratory for Materials Science
Institute of Metal Research
Chinese Academy of Sciences
Shenyang 110016, China
E-mail: jhqiu@imr.ac.cn

L. P. Wang
School of Materials Science and Engineering
University of Science and Technology of China
Shenyang 110016, China

J. X. Xia, M. K. Nazeeruddin
Institute of Chemical Sciences and Engineering
École Polytechnique Fédérale de Lausanne (EPFL)
CH-1951 Sion, Switzerland
E-mail: jianxing.xia@epfl.ch; mdkhaja.nazeeruddin@epfl.ch

Z. Yan
College of Energy and Environment
Shenyang Aerospace University
Shenyang 110136, China

P. Q. Song, Z. H. Wei
Institute of Luminescent Materials and Information Displays
College of Materials Science and Engineering
Huaqiao University
Xiamen 361021, China
E-mail: weizhanhua@hqu.edu.cn

G. Shao
School of Chemistry
Sun Yat-sen University
Guangzhou 510006, China

Z. L. Qiu
College of Materials and Chemistry and Chemical Engineering
Chengdu University of Technology
Chengdu 610059, China

To address these issues, different passivation molecules as modification layers were used in the buried interface of *n-i-p* structured PSCs, such as the ionic liquids, organic polymers and small molecules,[16–20] which markedly passivated the trap defects and improved the stability by the introduction of surface interaction with these defect charges or under-coordinated ionic components. In addition, researchers also modified the work function (W_F) of electron transport layers (ETLs) to regulate the mismatch of conduction band minimum (CBM) between ETLs and perovskites, thus alleviating the interface carrier recombination.[21,22] Nevertheless, these routes ignored the influence of the bulk defect induced recombination within perovskite films. Besides, most surface-treatment agents used in the passivation of such buried interface of PSCs can be washed away in the subsequent spin-coating processes of perovskite films. Developing a facile strategy to inhibit both interface and bulk carrier recombination should thus be considered. Meanwhile, building a robust passivation layer at the buried interface favors the carrier transport and the device performance.

Herein, we introduce a cation diffusible interface layer based on Potassium L-aspartate (PL-A) to inhibit both interface and bulk non-radiative carrier recombination in the buried interface of conventional *n-i-p* structured PSCs. Experiments and theories found that the K^+ cations of PL-A could diffuse into the perovskite layer and form a gradient *n*-doping after spin-coating. However, the anions remain at the SnO_2 surface through strong chemical adsorption, which modulates dipole moment towards ETL. As a result, the energy level structure near SnO_2/perovskite interface is well aligned, thus restraining the defect induced carrier recombination and simultaneously improving the carrier transport. As a result, a champion PCE of 23.74% was obtained for the PL-A modified small-area devices, with dramatically improved open-circuit voltage (V_{oc}) of 1.19 V. In comparison, the reference cell yielded 21.93% efficiency. The large-area devices (1.05 cm^2) achieved a PCE of 22.23%, extremely high values for large-area PSCs. Furthermore, the modified devices exhibited negligible hysteresis and enhanced ambient air stability.

2. Results and Discussion

The chemical structure of Potassium L-Aspartic (PL-A), which we used as an interfacial modifier is shown in Figure S1 (Supporting Information). In our experiment, the target film was fabricated with a spin-coating PL-A aqueous solution on the SnO_2 surface to reconstruct the SnO_2/PVK interface. Scanning electron microscopy (SEM) images shown in Figure S2 (Supporting Information) display the micromorphology of SnO_2 layers with and without PL-A treatment. As can be seen, there is no significant change after depositing PL-A, mainly because the modifier layer is too thin to be observed. To investigate the interaction between SnO_2 and PL-A, X-ray photoelectron spectroscopy (XPS) measurements were performed, and the results are depicted in **Figure 1**a–c and S3 (Supporting Information). The occurrence of N 1s (Figure S3c, Supporting Information) confirms the existence of PL-A on the SnO_2 surface. As shown in Figure 1a, Sn 3d$_{5/2}$ (486.66 eV) and Sn 3d$_{3/2}$ (495.06 eV) peaks of the pristine SnO_2 film shift to 487.03, 495.33 eV, respectively, after PL-A treatment, indicating the interaction between SnO_2

and PL-A. The O 1s spectrum of pristine SnO_2 film plotted in Figure 1b shows a broad asymmetric peak, which can be de-convoluted into lattice oxygen (530.66 eV) and chemisorbed oxygen atoms or hydroxyl groups (531.86 eV). The peak intensity of lattice oxygen is found to decrease while that of the adsorbed oxygen increases (Figure 1c), demonstrating the change in the chemical circumstance of oxygen atoms in the lattice of SnO_2 surface after the treatment, mainly induced by the interaction between SnO_2 surface and PL-A.[23]

We then conducted Fourier transform infrared (FTIR) spectroscopy measurements to further analyze their interaction. As shown in Figure 1d and Figure S4 (Supporting Information) the typical $-COO^-$ stretching vibration mode at ≈1610 cm^{-1} is observed in the PL-A spectrum. For the PL-A treated SnO_2 sample, a downshift to ≈1583 cm^{-1} is observed, again confirming the reaction between SnO_2 and $-COO^-$ on PL-A, in line with XPS results. To realize the interactions directly, a DFT calculation was further performed to study the adsorption behavior of PL-A molecule on the SnO_2. The SnO_2 (010) surface was used as the clean surface, and 20 Å vacuum layer was used to minimize the interaction between the periodic structure. As shown in Figure 1e, the optimized geometries show that the $-COO^-$ of the PL-A anion bonds with the exposed Sn atom of the SnO_2 and the amino group is towards the perovskite side. All the different configurations demonstrate the same behavior, which is consistent with the FTIR and XPS results. The Lewis acid-base coordination reaction between amino and PbI_2 by introducing amino-containing agents was widely applied in the modification of PVK.[24–26] We then investigated the interaction between PL-A and PbI_2. As illustrated in Figure S5 (Supporting Information), the Pb 4f XPS spectrum of pure PbI_2 exhibits two main peaks at 138.6 and 143.5 eV, corresponding to Pb 4f$_{7/2}$ and 4f$_{5/2}$, respectively. Two weaker peaks appear at around 136.9 and 141.7 eV, indicating the existence of metallic Pb (Pb^0). After being treated with PL-A, the peaks of Pb 4f$_{7/2}$ and 4f$_{5/2}$ shift to 138.4 and 143.2 eV, respectively, revealing the decreased cationic charge of under-coordinated Pb^{2+}. Meanwhile, the characteristic peaks of Pb^0 disappear after PL-A treatment, suggesting that the coordination reaction can inhibit the formation of Pb^0 defects. The N 1s spectrum displayed in Figure S5b shows a new peak appearing at ≈399.4 eV after the reaction of PL-A with PbI_2, verifying the acid-base coordination reaction between amino on the PL-A and PbI_2 where amino serves as Lewis base and PbI_2 acts as Lewis acid.

The crystal structure and micromorphology of PVK films fabricated on the pristine and PL-A treated SnO_2 films with different concentrations were investigated through X-ray diffraction (XRD) and scanning electron microscopy (SEM). As shown in Figure S6 (Supporting Information) the XRD patterns of different films are almost identical. And the SEM images in Figure S7 (Supporting Information) exhibit little difference as well. These results suggest that the PL-A treatment has little effect on PVK crystallization. Ultraviolet-visible (UV-vis) absorption spectra plotted in Figure S8 (Supporting Information) reveal that the light-harvesting properties of PVK films remain almost unchanged, and the bandgap is calculated to be 1.57 eV from the Tauc plots (insert in Figure S8, Supporting Information).

The interfacial materials might diffuse into the inside of PVK film because of the high solubility of DMF/DMSO
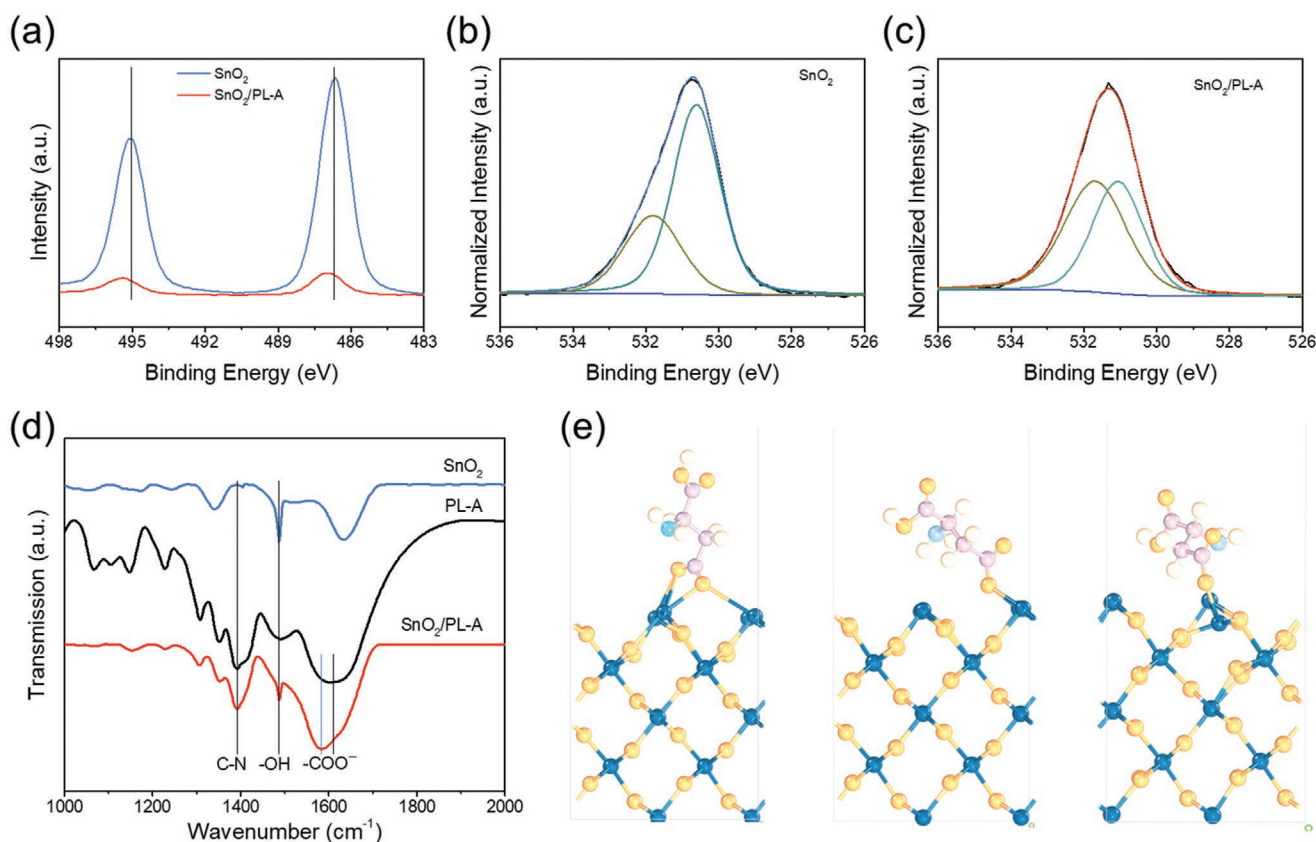
ADVANCED
SCIENCE NEWS
www.advancedsciencenews.com

ADVANCED
FUNCTIONAL
MATERIALS
www.afm-journal.de

Figure 1. a) The XPS of Sn $3d_{5/2}$ and Sn $3d_{3/2}$ of SnO_2 with or without the PL-A modification; b) The O 1 s spectrum of pristine SnO_2 film; c) The O 1 s spectrum of SnO_2 film modified by PL-A; d) The Fourier transform infrared spectroscopy of SnO_2 with or without the PL-A modification; e) The optimized geometries of PL-A adsorption on SnO_2 (010) surface, where the pink, yellow, light yellow, blue and light blue atoms respectively represent the C, O, H, Sn and N atoms.

solvent during film fabrication. Time of Flight Secondary Ion Mass Spectrometry (ToF-SIMS) measurements were further employed to analyze the vertical distribution of PL-A, of which the anion and cation distributions are respectively exhibited in **Figure 2**a,b.[27] The results plotted in Figure 2a reveal that the $COOH^-$ mainly distributes at SnO_2/PVK interface, manifesting that the PL-A anions could remain on the SnO_2 surface after PVK film spin-coating, mainly caused by the strong chemical adsorption on the SnO_2 surface by the metal-oxygen bonds (Figure 1). On the contrary, the K^+ cations (Figure 2b) are found to move into the PVK film and exhibit a gradient attenuation in the vertical direction of the film. For the reference devices, the K^+ cation signal is derived from the SnO_2 colloidal solution used in the SnO_2 ETL fabrication process.[28]

We further probed the influence of the chemical adsorption anions and the diffused cations on the energy level alignment in the buried interface. As shown in Figure S9 (Supporting Information) the DFT was employed to demonstrate the doping effect of K^+ cations within the PVK film, where the K^+ cations are prone to fill the absent surface vacancies of MA^+ and interact with the I atoms at the centre of the cuboctahedral halide cages, leading to surface coordination.[29] To realize the surface charge transfer, which usually implies the Fermi level shift, the charge density difference was further calculated by DFT. The red and yellow electron clouds represent the

electron electronic accumulation and depletion, respectively. When the K^+ cations enter the perovskite crystals, the electron will transfer from the surrounding cuboctahedral halide cages to the interacted K^+ cations, enhancing the surface electron concentration. The change of the electron concentration testifies to an n-type doping effect in PVK film, which is consistent with the result reported in the literature.[30] Combining with the gradually-decreasing of K^+ diffusion concentrations from ETL to HTL sides shown in TOF-SIMS spectra, there will be a gradually doping in the PVK film, which endows a homo-junction within the PVK film and provides an extra build-in field across the film, thus reinforcing the carriers transport and restricting the defective recombination in the PVK film. On the other side of the PL-A modified SnO_2/PVK interface, the SnO_2 (010) surface possesses a strong electron accumulation due to the PL-A supplied forward (− +) dipole moment (Figure S9a–c), in line with the results of XPS as discussed in Figure 1a. The higher surface electron concentration would up-shift the Fermi level of the SnO_2 and reduce the surface work function.

To verify the possible influence on energy level structure after this interface reconstruction, we executed ultraviolet photoelectron spectra (UPS) measurement, the cutoff (E_{cutoff}) and onset (E_i) energy regions, which are shown in Figure S10 (Supporting Information). For the SnO_2 surface, the E_i region (Figure S10a) shows that the energetic gap between E_F and
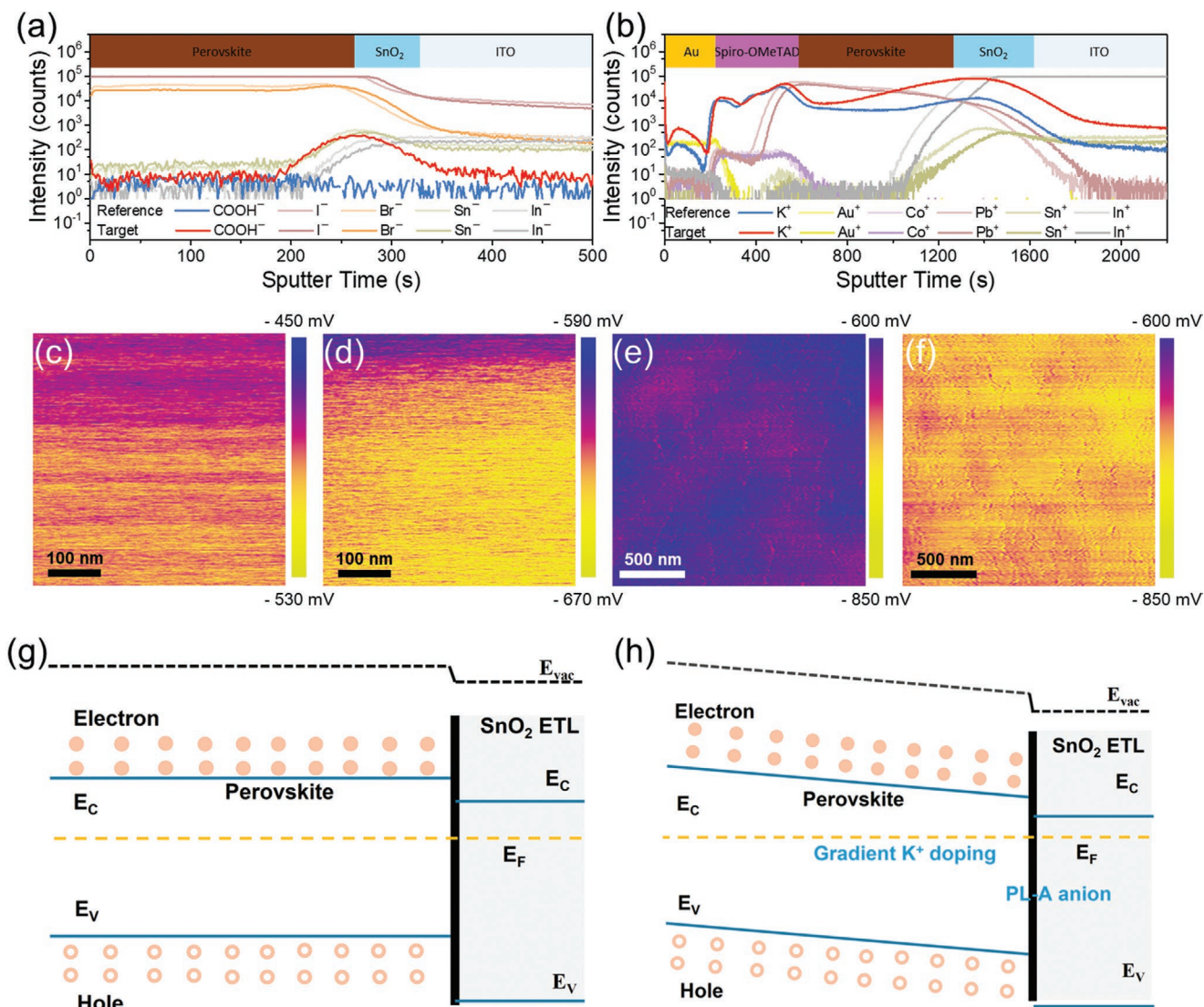
Figure 2. a) The ToF-SIMS of anion distribution within ITO/SnO$_2$/perovskite film; b) The ToF-SIMS of cation distribution within ITO/SnO$_2$/perovskite/Spiro-OMeTAD/Au devices; The KPFM of films based on SnO$_2$ c), SnO$_2$/PL-A d), SnO$_2$/thin perovskite e) and SnO$_2$/PL-A/thin perovskite f); g) The illustration of the energy level of the reference devices; h) The illustration of energy level of devices based on PL-A.

E_{vb} becomes extends from 3.44 to 3.62 eV after depositing the PL-A, affirming the electron accumulation on its surface, thereby decreasing the work function of the SnO$_2$ from 4.43 to 4.18 eV originated from the surface dipole moment from PL-A (Figure S10b). For the PVK thin film fabricated on the PL-A modified SnO$_2$ surface, it can be seen that the work function also decreases from 4.36 to 4.15 eV (Figure S10c,d), verifying the n-type doping of the PVK film by the diffusion of K$^+$ cations, agreeing well with the n-doping effect induced by the alkalis within PVK, which is also characterized by the DFT results mentioned above. To further reveal the electronic states of SnO$_2$ and PVK influenced by the PL-A modification, we adopted the Kelvin probe force microscope (KPFM) to measure the surface potential of thin PVK film and SnO$_2$ substrate with or without PL-A interlayer in Figure 2c–e, of which the corresponding atomic force microscope (AFM) results are shown

in Figure S11 (Supporting Information). The contact potential difference (CPD) of samples was measured, and the negative (positive) CPD shift illustrates the increased (decreased) E_F compared to that of the biased tip.[31] When PL-A is deposited on the SnO$_2$ film, the color of the potential image of SnO$_2$ changes from pink to orange with a decreased value from about ≈500 to ≈600 mV, indicating that the PL-A can reduce the work function of the SnO$_2$ surface owing to the surface electron accumulation caused by the surface electric dipole that can attract the electrons of SnO$_2$ film. For the thin PVK film, the sample modified with PL-A exhibits an orange color, while the reference film possesses a dark blue feature. The lower potential value of the PL-A modified sample reveals the n-doping of perovskite, consistent with the UPS and DFT results. Based on these experimental and simulative results, we depict the energy structure at the buried SnO$_2$/PVK interface in Figure 2g,h,
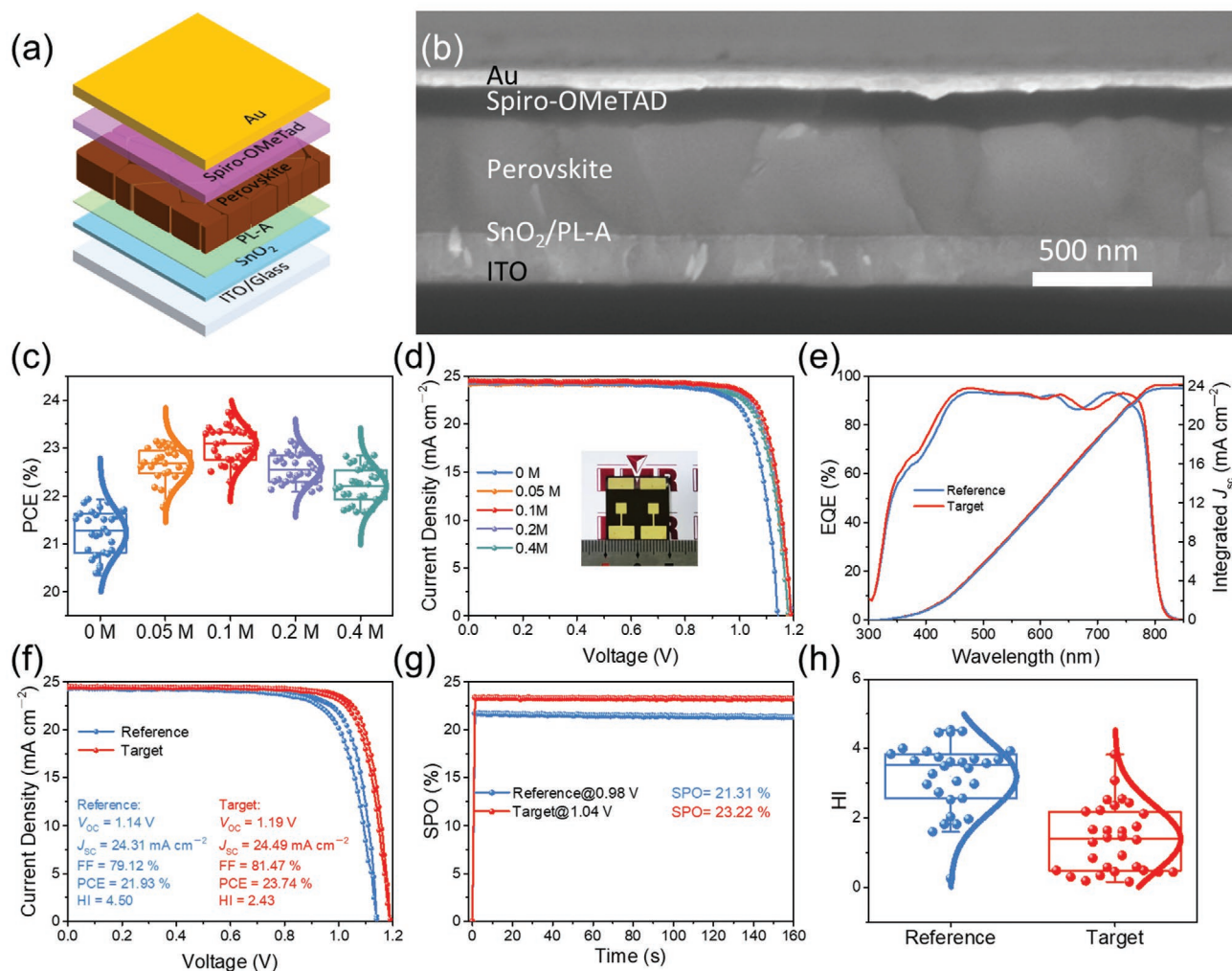
Figure 3. a) The illustration of devices construction based on ITO/SnO$_2$/PL-A/Perovskite/Spiro-OMeTAD/Au; b) The SEM of the devices based on ITO/SnO$_2$/PL-A/Perovskite/Spiro-OMeTAD/Au; c) The statistical efficiency of devices modified with various concentrations of PL-A; d) The J–V curves of devices based on various concentrations of PL-A; e) The IPCE of the device with or without the PL-A modification (0.1 M); f) The reverse and forward J–V curves of champion devices with or without the PL-A modification (0.1 M); g) The steady-state efficiency of devices with or without the PL-A modification (0.1 M) at maximum power output point; h) The statistical hysteresis of devices with or without the PL-A modification (0.1 M).

from which one can see that the homo-junction within the PVK induced by the gradient K$^+$ doping of the PL-A modified interface can provide an extra build-in field across the film, which facilitates the carrier transport and separation near the buried interface, further restraining the electron and hole recombination at the defective perovskite and ETL interface. Besides, compared to the original SnO$_2$/PVK interface, the PL-A modified one possesses a higher Fermi level, which could give rise to a larger difference between the quasi-Fermi energy levels of ETL/PVK and PVK/HTL interfaces, resulting in a predictable larger V_{oc} of the corresponding devices.

To verify the possible superior advantage ascribed to the PL-A interface modifier, we fabricated PSCs to elucidate the effect of this interface reconstruction on device performance. The typical n-i-p configuration of ITO/SnO$_2$/PVK/spiro-OMeTAD/Au was employed, and PL-A was introduced into the buried SnO$_2$/PVK interface, as illustrated in **Figure 3**a,b. Figure 3c shows statistical

photovoltaic performance with 30 devices depending on PL-A concentrations, and the photovoltaic parameters are summarized in Table S1(Supporting Information). The optimum concentration of PL-A is 0.1 M. Hereafter, the target devices are fabricated on SnO$_2$ substrates treated with 0.1 M PL-A. The J–V curves of the champion devices are shown in Figure 3d. As can be seen from these results, the effect of interface reconstruction is distinct since all performance parameters of target devices are improved substantially. The average short-circuit current density (J_{SC}) is increased from 24.29 to 24.32 mA cm^{-2}, and the integrated J_{sc} calculated from the corresponding incident photon-to-current conversion efficiency (IPCE) spectra are 23.78 and 24.13 mA cm^{-2} respectively (Figure 3e), in good agreement with J–V measurements. Compared with the reference sample, the IPCE values of the device with PL-A are slightly enhanced, especially in the range of 350–500 nm, leading to the enhanced integrated J_{sc}. Since the absorption properties of the perovskite films

ADVANCED
SCIENCE NEWS
www.advancedsciencenews.com

ADVANCED
FUNCTIONAL
MATERIALS
www.afm-journal.de

are almost unaffected by the introduction of PL-A (Figure S8), such increase in IPCE could be ascribed to the reduction of recombination loss, which benefits from the optimized interfacial energy level structure (Figure 2h) and the passivation on the defects near the buried interface (Figure S5). The average V_{oc} increases from 1.14 to 1.19 V with a nearly unchanged PVK bandgap, meaning the largely reduced V_{oc} deficit. Besides, an increase in fill factor (FF) from 76.48 to 80.06% is also observed. The reduced V_{oc} deficit and increased FF also imply a suppressed interface recombination, confirming the better carrier transport feature after the interface reconstruction. In the combination of these advancements, the average PCE prominently increases from 21.23 to 23.08%, with champion values of 21.93 and 23.74%, respectively (Figure 3f). The champion devices' stabilized power output (SPO) was then tested to evaluate their efficiency reliability. As can be seen from Figure 3g, the stable efficiency is 23.22 and 21.31% for the target and reference devices, respectively, well in line with the J–V measurements. Note that this interface reconstruction also alleviates hysteresis; the hysteresis index (HI) calculated by the formula of HI = (PCE$_{RS}$ − PCE$_{FS}$)/PCE$_{RS}$ shows a significantly decline from 3.19 to 1.39 (Figure 3h), which can be attributed to the efficient carrier transport at the PL-A modified SnO$_2$/PVK interface.[32]

Steady-state photoluminescence (PL) spectra were measured to understand carrier dynamics with fabricating PVK films on the glass or glass/ITO/SnO$_2$ substrate, and the target films were treated by PL-A before depositing PVK. As illustrated in **Figure 4**a, the target film fabricated on the glass substrate shows higher PL intensity than that of the reference one,

revealing a suppressed non-radiative recombination at the buried interface. In PSCs, the uncoordinated defects at the interface are usually considered to be recombination centres, resulting in severe non-radiative recombination. As discussed above, the amino group on PL-A can coordinate with PbI$_2$ and reduces the formation of Pb^0 defects. At the same time, the COO- of the PL-A anion can bond with the exposed Sn atom of the SnO$_2$ surface, leading to a decreased amount of uncoordinated Sn defects on the SnO$_2$ surface. As a result, the target film tread with PL-A interface modifier fabricated on glass substrate shows reduced non-radiative recombination and higher PL intensity. The PL quenching behavior of the film fabricated on glass/ITO/SnO$_2$ substrate is quite different. The target film exhibits an obviously lower PL intensity than that of the reference one, implying higher carrier extraction efficiency at the buried interface, which can be attributed to the passivation on the defects near the interface by the introduction of PL-A and the enhanced carriers transport by the regulation of interfacial energy structure as discussed above. Time-resolved photoluminescence (TRPL) measurement was also performed with fabricating PVK films on glass/ITO/SnO$_2$ substrates, and the PL intensity decay curves plotted in Figure 4b are fitted with a bi-exponential decay equation:

$$I(t) = I_0 + A_1 e^{-t/\tau_1} + A_2 e^{-t/\tau_2} \tag{1}$$

where the fast τ_1 decay component corresponds to charge extraction, and the slow τ_2 component represents radiative recombination from the bulk PVK. Compared to the reference film (τ_1 = 11.79 ns), the lifetime determined on fast decay traces
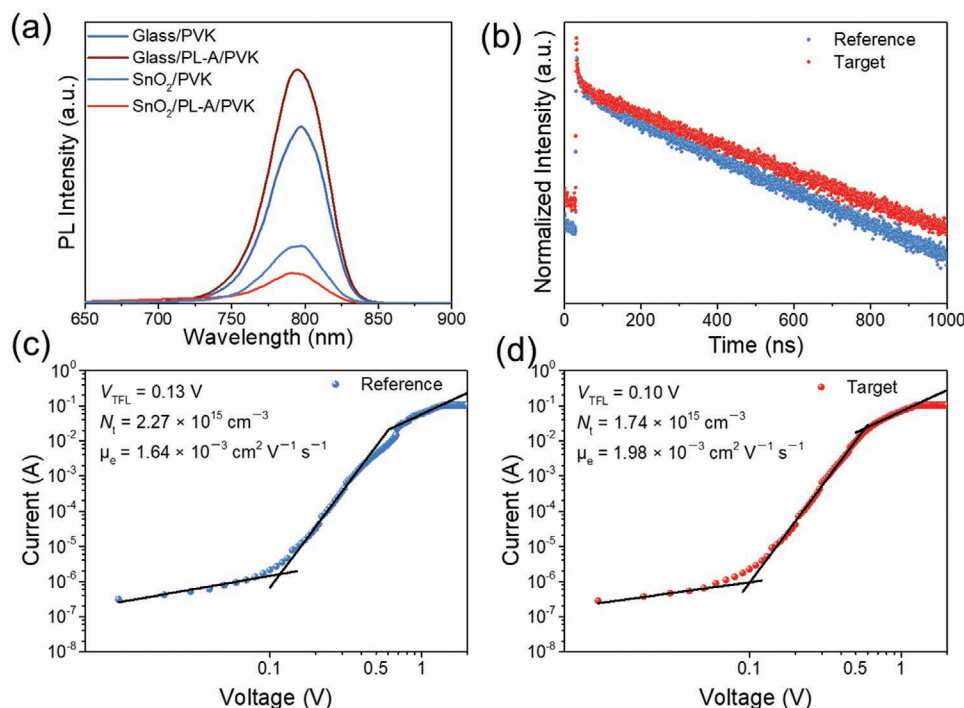

Figure 4. a) The PL of films based on Glass/Perovskite, Glass/PL-A/Perovskite, SnO$_2$/Perovskite and SnO$_2$/PL-A/Perovskite; b) The TRPL of films based on SnO$_2$/Perovskite and SnO$_2$/PL-A/Perovskite; c) and d) respectively are SCLC measurements based on electron-only devices with ITO/SnO$_2$/ with or without PL-A/PVK/PCBM/Ag structures.
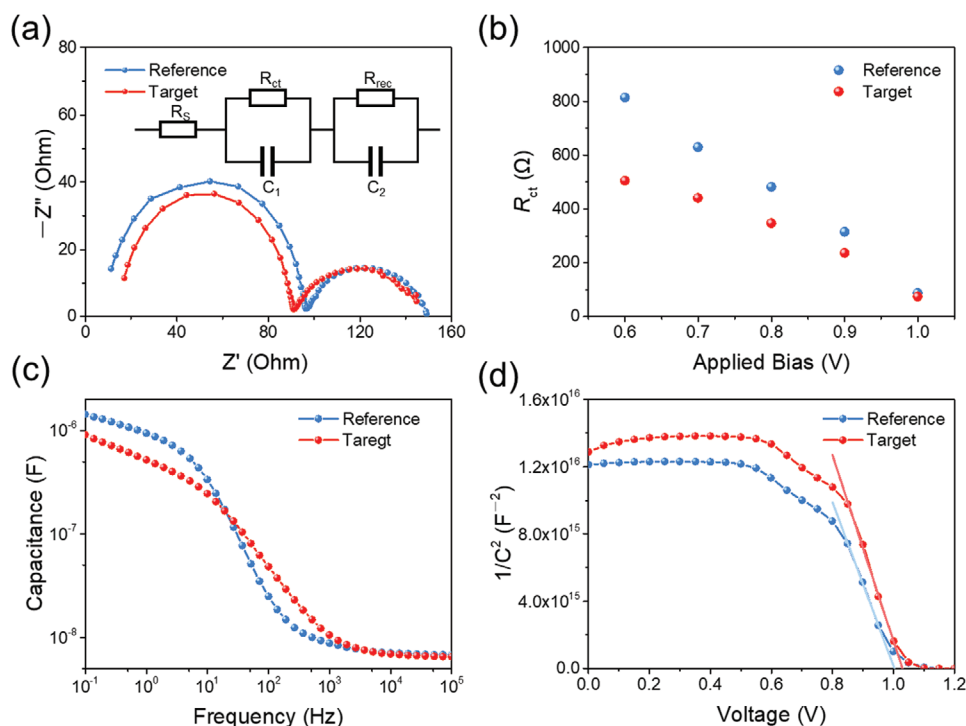
Figure 5. a) Nyquist plots of devices with and without interface reconstruction, which were tested under illumination by applying a bias voltage of 1.0 V; b) The fitted R_{ct} under different biases; c) The capacitance-frequency ($C–f$) measurements of samples with or without the PL-A; d) Mott-Schottky plots as a function of applied bias at 10 KHz for the cells with or without the PL-A modification under dark conditions.

of the target film is significantly reduced to 7.41 ns ($\tau_1 = 7.41$ ns). In addition, the slow τ_2 component is found to slightly increase from 839.88 to 932.93 ns after interface reconstruction with nearly unchanged crystallization and micromorphology of synthesized PVK films, indicating a declined amount of defects in bulk PVK. Space charge limited current (SCLC) measurements based on electron-only devices with ITO/SnO$_2$/with or without PL-A/PVK/PCBM/Ag structure were executed to evaluate the trap density (N_t) and electron mobility (μ_e) as illustrated in Figure 4c,d. Generally, the J−V curves display three distinctive regimes. At low bias, the current varies linearly with voltage, and the slope of the curve is 1, indicating an ohmic contact. With the bias voltage increase, the curves gradually enter the trap-filled limited (TFL) regime, in which the injected carriers start to fill the traps, and the curve slope is over 3. The TFL voltage (V_{TFL}) is determined as the intersection voltage of ohmic and TFL regimes and can be used to derive N_t with the equation:

$$N_t = \frac{2\varepsilon_0\varepsilon V_{TFL}}{eL^2} \tag{2}$$

where ε_0 and ε are the vacuum permittivity and the relative permittivity of PVK, respectively, e is the elementary charge, and L is the thickness of PVK film. As can be seen, the N_t values decrease from 2.27×10^{15} to 1.74×10^{15} cm^{-3} after interface reconstruction, which is ascribable to the coordination between PL-A and PbI$_2$. The reduction of defects density is beneficial to suppressing non-radiative recombination, thus improving the device performance. At the SCLC regime where the curve slope

is 2 at the higher bias voltage region, the μ_e can be calculated with Mott-Gurney Law:

$$J = \frac{9}{8}\varepsilon_0\varepsilon\mu \frac{V^2}{L^3} \tag{3}$$

Compared with the reference ($\mu_e = 1.64 \times 10^{-3}$ cm^2 V^{-1} s^{-1}), the device with interface reconstruction exhibits higher electron mobility of 1.98×10^{-3} cm^2 V^{-1} s^{-1}, which can mainly be deduced to the reduced amounts of traps in the film, giving rise to a better electron transport prospective, then thus improving the device performance as revealed in J−V measurement.

Electrochemical impedance spectroscopy (EIS) measurements were performed to obtain more information about carrier transport behavior and interfacial properties. **Figure 5**a illustrates the Nyquist plots of devices with and without PL-A interface reconstruction, which were tested under illumination by applying a bias voltage of 1.0 V. As can be seen, the Nyquist plots consist of two semicircles located at different frequency ranges. Generally, the high-frequency component corresponds to the charge transport resistance (R_{ct}), and the low-frequency component is related to the recombination resistance (R_{rec}). The fitted R_{ct} under different biases is plotted in Figure 5b. The R_{ct} value of the target device is decreased, demonstrating better charge transport properties. In addition, the R_{rec} is found to be slightly increased in the target device (Figure S12, Supporting Information), which suggests that the recombination is restricted after the introduction of PL-A interface modifier. The capacitance-frequency (C−f) measurements were then conducted to further evaluate the carrier transport properties, and

the result is plotted in Figure 5c. Generally, the capacitance in low-frequency regime is associated with charge accumulation at the interface. After interface reconstruction, the capacitance in low frequency is significantly reduced, indicating a restrained interfacial charge accumulation contributed by the better carrier transport properties. As a result, the device with interface reconstruction exhibits superior performance, and meanwhile, the hysteresis is alleviated as well.

Mott-Schottky (M-S) plots were also collected at 10 kHz to investigate the interfacial properties, from which the charge density and build-in potential (V_{bi}) can be calculated with the equation:

$$\frac{1}{C^2} = \frac{2(V_{bi} - V)}{A^2 q \varepsilon_0 \varepsilon N} \tag{4}$$

Where A represents the active area of the device and N is the charge density. By fitting the voltage dependence of the 1 C^{-2} curves shown in Figure 5d, one can see that the slope of the device with interface reconstruction is larger, indicating the lower charge density, proving the less charge accumulation at the interface as revealed in C–f measurements. Furthermore, the device demonstrates an increased V_{bi} of 1.03 V after interface reconstruction compared with the reference one of 1 V. There are two reasons which can give rise to an improved build-in potential. One is the up-shifted Fermi levels at the buried SnO$_2$/PVK interface as illustrated in Figure 2g,h, caused by the chemical interaction between PL-A and SnO$_2$/PVK surfaces.

Another is the extra build-in field induced by the n-type doping effect of the K$^+$ diffusion gradient (Figure 2h). The higher V_{bi} of PL-A modified device implies the optimized regulation of interfacial energy structure, thus contributing to the substantially increased V_{oc} as exhibited in J–V measurements.

Furthermore, this PL-A based interface reconstruction method was employed for the fabrication of large-area PSCs, whose performances are more severely dragged by defects due to the challenge in fabricating uniform large-area PVK films via the spin-coating method. The statistical result of 20 devices shown in **Figure 6**a indicates that the performance improvement for large-area devices (1.05 cm^2) is more notable. The devices with interface reconstruction achieve an average PCE of 21.23% (22.23% for champion with V_{oc} of 1.19 V, J_{sc} of 24.24 mA cm^2, and FF of 77.08%), significantly higher than that of the reference ones (19.25% on average and 20.08 for champion with V_{oc} of 1.14 V, J_{sc} of 24.23 mA cm^2, and FF of 72.71%). Figure 6b illustrates the J–V curves of champion devices before and after PL-A interface reconstruction, one can see that the FF exhibits an impressive improvement after the interface reconstruction. The large-area devices typically suffer more from trap-assisted non-radiative recombination. But our PL-A based interface reconstruction can effectively passivate the defects near the SnO$_2$/PVK interface and build an optimized interfacial energy structure to assist the carriers in escaping from defect capture, as discussed above. Consequently, better carrier transport characteristic is obtained, finally giving rise to higher device performance. The champion device with interface
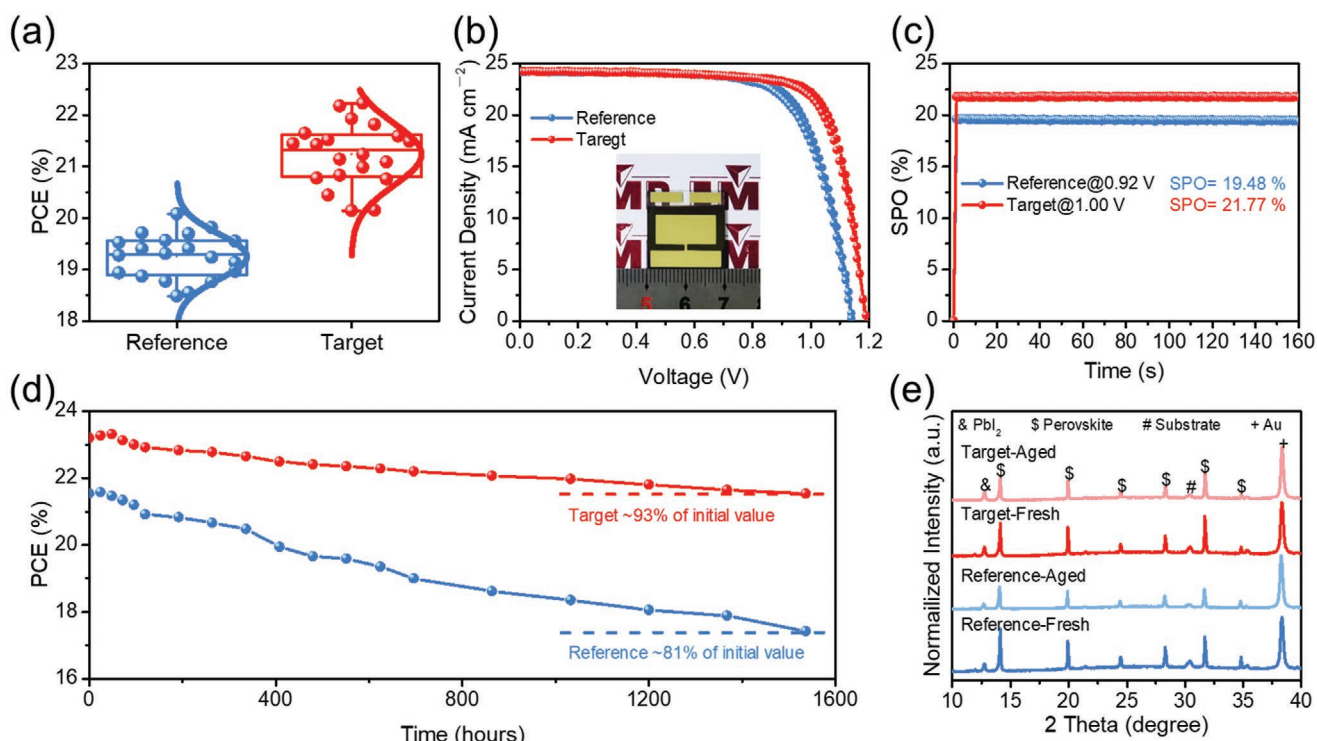

Figure 6. a) The statistical efficiency of large-area devices (1.05 cm^2) with or without PL-A (0.1 M); b) The J-V curves of champion large-area devices (1.05 cm^2) with or without PL-A (0.1 M); c) The steady-state efficiency of large-area devices (1.05 cm^2) with or without the PL-A modification (0.1 M) at maximum power output point; d) The stability of devices with or without PL-A (0.1 M) under ambient conditions (≈20% RH); e) The XRD of fresh and aged devices with or without the PL-A modification.

reconstruction gives a SPO of 21.77%, obviously higher than that of the reference one (19.48%). The long-term stability is also the key metric for PSCs toward applications. Thus the stability of unencapsulated devices was tested under ambient conditions (≈20% RH) with shielding the light, and the results are plotted in Figure 6d. The device with interface reconstruction exhibits superior stability, remaining about 93% of initial PCE with over 1500 h ageing, whereas the reference one only remains ≈81%.

To probe the mechanism of the improved stability induced by the PL-A interface modifier, the changes in perovskite crystal characteristics of fresh and aged devices were performed by XRD in Figure 6e. Both of the aged devices with or without PL-A interface reconstruction show almost invariable PbI_2 diffraction peaks as compared to the fresh devices, indicating the high stability of perovskite crystals during the ageing period and the little influence of moisture on the synthesized PVK films. Except the external factor, the ionic migration issue has attracted wide investigations through experimental and theoretical methods because it plays crucial role in the decline of the device performance of PSCs during ageing. It demonstrates that the MA^+/FA^+ cations of perovskite are easy to migrate via the vacancy defects even at room temperature due to the much low activation energy for migration.[33,34] By employing the PL-A interface modifier, the surface vacancies of SnO_2 and PVK are effectively passivated by their interactions with PL-A radicals, as discussed above, which helps to suppress the escape of organic ions in the perovskite lattices. In addition, the introduction of K^+ cations by the solvation of PL-A in PVK solution could effectively passivate the bulk defects of PVK film, giving rise to the restrain in the formation of ion migration channels.[35–37] Moreover, the charge accumulation issue at ETL/PVK interface that presumably results in much faster degradation of device performance is effectively suppressed by the improved carrier transport at the PL-A modifier reconstructed interface. The inhibition of the ionic migration and charge accumulation finally improves the intrinsic stability of the PL-A-based PSCs.

3. Conclusion

In summary, we develop an interfacial diffusion doping strategy to improve the performance of SnO_2-based PSCs by reconstructing energy level alignment for the transport of photogenerated carriers in the buried interface. The results find that the anions of PL-A can remain at the SnO_2 surface via strong chemical adsorption to build a robust interface modifier. In contrast, the metal cations diffuse into perovskite, leading to a gradient *n*-doping in perovskite near the SnO_2/ perovskite interface. The extra surface dipole moment supplied by the remained anions and the gradient *n*-doping by the diffused potassium cations reconstruct the energy level structure near the buried interface, reinforcing the carrier's escape at the under-coordinated defects and accelerating the carrier transfer at the interface. Besides, the effective passivation of defects near the buried interface and the improved transport features of photogenerated carriers could inhibit the ionic migration and charge accumulation issues, thus improving the stability of the fabricated devices. Finally, the devices based on the PL-A interface modifier achieved a PCE of 23.74% for small-area devices with a high V_{oc} of 1.19 V and a PCE of 22.23% for large-area devices (1.05 cm^2), which exhibited excellent stability without encapsulation.

Conflict of Interest

The authors declare no conflict of interest.

Data Availability Statement

The data that support the findings of this study are available from the corresponding author upon reasonable request.

[1] J.-H. Im, C.-R. Lee, J.-W. Lee, S.-W. Park, N.-G. Park, *Nanoscale* **2011**, *3*, 4088.

[2] G. Hodes, *Science* **2013**, *342*, 317.

[3] J. Burschka, N. Pellet, S.-J. Moon, R. Humphry-Baker, P. Gao, M. K. Nazeeruddin, M. Grätzel, *Nature* **2013**, *499*, 316.

[4] J. H. Noh, S. H. Im, J. H. Heo, T. N. Mandal, S. I. Seok, *Nano Lett.* **2013**, *13*, 1764.

[5] A. Kojima, K. Teshima, Y. Shirai, T. Miyasaka, *J. Am. Chem. Soc.* **2009**, *131*, 6050.

[6] G. Xing, N. Mathews, S. Sun, S. S. Lim, Y. M. Lam, M. Grätzel, S. Mhaisalkar, T. C. Sum, *Science* **2013**, *342*, 344.

[7] Best Research-Cell Efficiency Chart, https://www.nrel.gov/pv/cell-efficiency.html (accessed: April 2022).

[8] J. Peng, Y. Wu, W. Ye, D. A. Jacobs, H. Shen, X. Fu, Y. Wan, T. Duong, N. Wu, C. Barugkin, H. T. Nguyen, D. Zhong, J. Li, T. Lu, Y. Liu, M. N. Lockrey, K. J. Weber, K. R. Catchpole, T. P. White, *Energy Environ. Sci.* **2017**, *10*, 1792.

[9] T.-H. Han, S. Tan, J. Xue, L. Meng, J.-W. Lee, Y. Yang, *Adv. Mater.* **2019**, 1803515.

[10] X. Zheng, B. Chen, J. Dai, Y. Fang, Y. Bai, Y. Lin, H. Wei, X. C. Zeng, J. Huang, *Nat. Energy* **2017**, *2*, 17102.

[11] J. Ye, C. Liu, D. Mei, Q. Ge, *ACS Catal.* **2013**, *3*, 1296.

[12] K. Liu, S. Chen, J. Wu, H. Zhang, M. Qin, X. Lu, Y. Tu, Q. Meng, X. Zhan, *Energy Environ. Sci.* **2018**, *11*, 3463.

[13] T. W. Jones, A. Osherov, M. Alsari, M. Sponseller, B. C. Duck, Y.-K. Jung, C. Settens, F. Niroui, R. Brenes, C. V. Stan, Y. Li, M. Abdi-Jalebi, N. Tamura, J. E. Macdonald, M. Burghammer, R. H. Friend, V. Bulović, A. Walsh, G. J. Wilson, S. Lilliu, S. D. Stranks, *Energy Environ. Sci.* **2019**, *12*, 596.

[14] S. A. L. Weber, I. M. Hermes, S.-H. Turren-Cruz, C. Gort, V. W. Bergmann, L. Gilson, A. Hagfeldt, M. Graetzel, W. Tress, R. Berger, *Energy Environ. Sci.* **2018**, *11*, 2404.

[15] Z. Liu, Q. Chen, J.-W. Lee, Z. Zhao, X. Xu, Y.-T. Hsieh, L. Meng, P. Sun, N. D. Marco, H. Zhou, Y.-B. Cheng, Y. Yang, *Adv. Energy Mater.* **2018**, *8*, 1800568.

[16] R. Wang, J. Xue, K.-L. Wang, Z.-K. Wang, Y. Luo, D. Fenning, G. Xu, S. Nuryyeva, T. Huang, Y. Zhao, J. L. Yang, J. Zhu, M. Wang, S. Tan, I. Yavuz, K. N. Houk, Y. Yang, *Science* **2019**, *366*, 1509.

[17] X. Wu, Y. Jiang, C. Chen, J. Guo, X. Kong, Y. Feng, S. Wu, X. Gao, X. Lu, Q. Wang, G. Zhou, Y. Chen, J.-M. Liu, K. Kempa, J. Gao, *Adv. Funct. Mater.* **2020**, *30*, 1908613.

[18] M. Kim, S. G. Motti, R. Sorrentino, A. Petrozza, *Energy Environ. Sci.* **2018**, *11*, 2609.

[19] L. Shi, H. Yuan, X. Sun, X. Li, W. Zhu, J. Wang, L. Duan, Q. Li, Z. Zhou, Z. Huang, X. Ban, D. Zhang, *ACS Appl. Energy Mater.* **2021**, *4*, 10584.

[20] C. Huang, P. Lin, N. Fu, K. Sun, M. Ye, C. Liu, X. Zhou, L. Shu, X. Hao, B. Xu, X. Zeng, Y. Wang, S. Ke, *J. Mater. Chem. A* **2018**, *6*, 22086.

[21] D. Yang, X. Zhou, R. Yang, Z. Yang, W. Yu, X. Wang, C. Li, S. (F.) Liu, R. P. H. Chang, *Energy Environ. Sci.* **2016**, *9*, 3071.

[22] K. Choi, J. Lee, H. I. Kim, C. W. Park, G.-W. Kim, H. Choi, S. Park, S. A. Park, T. Park, *Energy Environ. Sci.* **2018**, *11*, 3238.

[23] J. Chen, X. Zhao, S.-G. Kim, N.-G. Park, *Adv. Mater.* **2019**, *31*, 1902902.

[24] J.-Y. Seo, T. Matsui, J. Luo, J.-P. Correa-Baena, F. Giordano, M. Saliba, K. Schenk, A. Ummadisingu, K. Domanski, M. Hadadian, A. Hagfeldt, S. M. Zakeeruddin, U. Steiner, M. Grätzel, A. Abate, *Adv. Energy Mater.* **2016**, *6*, 1600767.

[25] W.-Q. Wu, Z. Yang, P. N. Rudd, Y. Shao, X. Dai, H. Wei, J. Zhao, Y. Fang, Q. Wang, Y. Liu, Y. Deng, X. Xiao, Y. Feng, J. Huang, *Sci. Adv.* **2019**, *5*, eaav8925.

[26] R. Chen, J. Cao, Y. Wu, X. Jing, B. Wu, N. Zheng, *Adv. Mater. Interfaces* **2017**, *4*, 1700897.

[27] J. A. Christians, P. Schulz, J. S. Tinkham, T. H. Schloemer, S. P. Harvey, B. J. Tremolet de Villers, A. Sellinger, J. J. Berry, J. M. Luther, *Nat. Energy* **2018**, *3*, 68.

[28] T. Bu, J. Li, F. Zheng, W. Chen, X. Wen, Z. Ku, Y. Peng, J. Zhong, Y.-B. Cheng, F. Huang, *Nat. Commun.* **2018**, *9*, 4609.

[29] S. You, H. Wang, S. Bi, J. Zhou, L. Qin, X. Qiu, Z. Zhao, Y. Xu, Y. Zhang, X. Shi, H. Zhou, Z. Tang, *Adv. Mater.* **2018**, *30*, 1706924.

[30] J. Zhang, R. Chen, Y. Wu, M. Shang, Z. Zeng, Y. Zhang, Y. Zhu, L. Han, *Adv. Energy Mater.* **2018**, *8*, 1701981.

[31] J.-H. Lee, J. Kim, G. Kim, D. Shin, S. Y. Jeong, J. Lee, S. Hong, J. W. Choi, C.-L. Lee, H. Kim, Y. Yi, K. Lee, *Energy Environ. Sci.* **2018**, *11*, 1742.

[32] X. Li, Y. Meng, R. Liu, Z. Yang, Y. Zeng, Y. Yi, W. E. I. Sha, Y. Long, J. Yang, *Adv. Energy Mater.* **2021**, *11*, 2102844.

[33] A. Walsh, S. D. Stranks, *ACS Energy Lett.* **2018**, *3*, 1983.

[34] Y. Hou, X. Du, S. Scheiner, D. P. McMeekin, Z. Wang, N. Li, M. S. Killian, H. Chen, M. Richter, I. Levchuk, N. Schrenker, E. Spiecker, T. Stubhan, N. A. Luechinger, A. Hirsch, P. Schmuki, H.-P. Steinrück, R. H. Fink, M. Halik, H. J. Snaith, C. J. Brabec, *Science* **2017**, *358*, 1192.

[35] J. Cao, S. X. Tao, P. A. Bobbert, C.-P. Wong, N. Zhao, *Adv. Mater.* **2018**, *30*, 1707350.

[36] D.-Y. Son, S.-G. Kim, J.-Y. Seo, S.-H. Lee, H. Shin, D. Lee, N.-G. Park, *J. Am. Chem. Soc.* **2018**, *140*, 1358.

[37] L. Wang, G. Wang, Z. Yan, J. Qiu, C. Jia, W. Zhang, C. Zhen, C. Xu, K. Tai, X. Jiang, S. Yang, *Sol. RRL* **2020**, *4*, 2000098.